



# Hyperfine and Nuclear Quadrupole Tensors of Nitrogen Donors in the $Q_A$ Site of Bacterial Reaction Centers: Correlation of the Histidine $N_\delta$ Tensors with Hydrogen Bond Strength

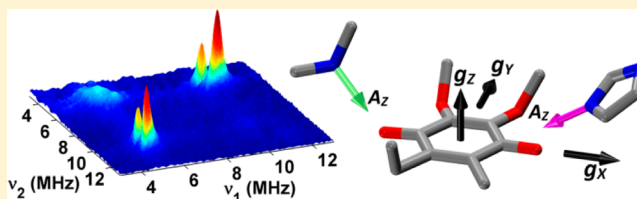
Alexander T. Taguchi,<sup>†</sup> Patrick J. O'Malley,<sup>\*,‡</sup> Colin A. Wraight,<sup>\*,†,§</sup> and Sergei A. Dikanov<sup>\*,||</sup>

<sup>†</sup>Center for Biophysics and Computational Biology, <sup>§</sup>Department of Biochemistry, and <sup>||</sup>Department of Veterinary Clinical Medicine, University of Illinois at Urbana—Champaign, Urbana, Illinois 61801, United States

<sup>‡</sup>School of Chemistry, The University of Manchester, Manchester M13 9PL, U.K.

## S Supporting Information

**ABSTRACT:** X- and Q-band pulsed EPR spectroscopy was applied to study the interaction of the  $Q_A$  site semiquinone ( $SQ_A$ ) with nitrogens from the local protein environment in natural abundance  $^{14}\text{N}$  and in  $^{15}\text{N}$  uniformly labeled photosynthetic reaction centers of *Rhodobacter sphaeroides*. The hyperfine and nuclear quadrupole tensors for His-M219  $N_\delta$  and Ala-M260 peptide nitrogen ( $N_p$ ) were estimated through simultaneous simulation of the Q-band  $^{15}\text{N}$  Davies ENDOR, X- and Q-band  $^{14,15}\text{N}$  HYSCORE, and X-band  $^{14}\text{N}$  three-pulse ESEEM spectra, with support from DFT calculations. The hyperfine coupling constants were found to be  $a(^{14}\text{N}) = 2.3$  MHz,  $T = 0.3$  MHz for His-M219  $N_\delta$  and  $a(^{14}\text{N}) = 2.6$  MHz,  $T = 0.3$  MHz for Ala-M260  $N_p$ . Despite that His-M219  $N_\delta$  is established as the stronger of the two H-bond donors, Ala-M260  $N_p$  is found to have the larger value of  $a(^{14}\text{N})$ . The nuclear quadrupole coupling constants were estimated as  $e^2Qq/4h = 0.38$  MHz,  $\eta = 0.97$  and  $e^2Qq/4h = 0.74$  MHz,  $\eta = 0.59$  for His-M219  $N_\delta$  and Ala-M260  $N_p$ , respectively. An analysis of the available data on nuclear quadrupole tensors for imidazole nitrogens found in semiquinone-binding proteins and copper complexes reveals these systems share similar electron occupancies of the protonated nitrogen orbitals. By applying the Townes–Dailey model, developed previously for copper complexes, to the semiquinones, we find the asymmetry parameter  $\eta$  to be a sensitive probe of the histidine  $N_\delta$ –semiquinone hydrogen bond strength. This is supported by a strong correlation observed between  $\eta$  and the isotropic coupling constant  $a(^{14}\text{N})$  and is consistent with previous computational works and our own semiquinone–histidine model calculations. The empirical relationship presented here for  $a(^{14}\text{N})$  and  $\eta$  will provide an important structural characterization tool in future studies of semiquinone-binding proteins.



## INTRODUCTION

The reaction center (RC) of the purple photosynthetic bacterium, *Rhodobacter (Rb.) sphaeroides*, facilitates electron transfer through a series of cofactors upon light activation. The final two cofactors occupying the  $Q_A$  and  $Q_B$  sites are chemically identical ubiquinone-10 (UQ-10) molecules. However, differences in the protein environment of the quinone sites result in significantly different roles for  $Q_A$  and  $Q_B$ .<sup>1–7</sup> Although  $Q_B$  allows for rapid association and dissociation of quinone and quinol,  $Q_A$  is a tightly bound prosthetic group. Light-induced charge separation at a dimer of bacteriochlorophyll followed by electron transport through a bacteriopheophytin results in the  $Q_A$  semiquinone state  $Q_A^{\cdot-}$  ( $SQ_A$ ).  $Q_A$  only undergoes one-electron chemistry and, upon formation of  $SQ_A$ , quickly transfers its electron to  $Q_B$ .

From the known structures of bacterial RCs, the  $C_4$  carbonyl of  $Q_A$  is hydrogen-bonded to  $N_\delta$  of His-M219 (which is also a ligand of a high spin nonheme  $\text{Fe}^{2+}$ ), whereas the backbone peptide nitrogen ( $N_p$ ) of Ala-M260 is the H-bond donor to the  $C_1$  carbonyl (Figure 1).<sup>6,8</sup> However, available X-ray structures do not provide an unequivocal description of the quinone site,

and the H-bond distances and torsional angles of the two methoxy substituents on the ubiquinone rings are quite variable across different structures.<sup>7</sup>

The interaction of a bound  $SQ$  intermediate with the protein environment can be specifically revealed through the application of high-resolution EPR methods.<sup>7,10–13</sup> Hydrogen bonding between protein nitrogens and quinone carbonyl oxygens is a typical structural motif in quinone processing sites. All of the  $SQ$ s studied thus far are involved in H-bond formation with at least one nitrogen.<sup>13</sup>

The H-bonds between  $SQ_A$  and its nitrogen donors in Zn-substituted RCs of *Rb. sphaeroides* strain R26 were characterized previously by 1D ESEEM at X (9.30 GHz) and C (7.23 GHz) microwave bands.<sup>14,15</sup> The ESEEM spectra at the two microwave frequencies showed interactions of the unpaired electron of  $SQ_A$  with two nitrogen nuclei in the protein. From analysis of the experimental data, tensors with  $^{14}\text{N}$  nuclear

Received: May 23, 2014

Revised: July 11, 2014

Published: July 15, 2014

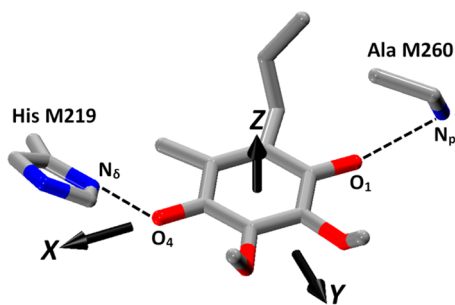


**Figure 1.** Interaction of SQ<sub>A</sub> with His-M219 N<sub>δ</sub> and Ala-M260 N<sub>p</sub>, which are H-bonded to carbonyl oxygens O<sub>4</sub> and O<sub>1</sub>, respectively. The principal axes of the *g*-tensor are labeled as X, Y, and Z. The *g<sub>X</sub>* axis lies along the line connecting the two oxygen atoms, which carry about half of the spin density, the *g<sub>Z</sub>* axis is perpendicular to the molecular plane, and *g<sub>Y</sub>* is perpendicular to both the other principal axes. The principal values of the SQ<sub>A</sub> *g*-tensor are *g<sub>X</sub>* = 2.00649, *g<sub>Y</sub>* = 2.00532, and *g<sub>Z</sub>* = 2.00210.<sup>9</sup>

quadrupole interactions  $e^2qQ/h = 1.52$  MHz,  $\eta = 0.82$ , and  $e^2qQ/h = 3.04$  MHz,  $\eta = 0.66$  were determined and assigned to N<sub>δ</sub> of His-M219 and N<sub>p</sub> of Ala-M260, respectively, on the basis of the quadrupole coupling constant  $e^2qQ/h$ . However, the limited resolution of the 1D spectra left significant uncertainties regarding the double-quantum correlation frequencies for both nitrogens which are important for estimating the hyperfine coupling strength.

Previously, we took advantage of the increased resolution from the 2D approach, and reported preliminary X-band <sup>14,15</sup>N 2D ESEEM spectra of SQ<sub>A</sub>.<sup>16</sup> However, a quantitative analysis of the data providing the principal values of the hyperfine and nuclear quadrupole tensors of the H-bonded nitrogens and their corresponding principal directions has yet to be performed. The lack of this information prevents an understanding of how the SQ spin density delocalizes into the protein environment and limits the usefulness of computational approaches exploring different structural models of the Q<sub>A</sub> site.

In this work we supplement the X-band <sup>14,15</sup>N 1D and 2D ESEEM spectra of SQ<sub>A</sub> with orientation selective ESEEM and ENDOR experiments performed at Q-band (~34 GHz) to determine the hyperfine interaction (hfi) and nuclear quadrupole interaction (nqi) tensors with the nitrogen H-bond donors His-M219 N<sub>δ</sub> and Ala-M260 N<sub>p</sub>. The hfi and nqi coupling constants, obtained by simulating the spectra simultaneously with the same parameter set, provide insight into H-bond strength and geometry at the Q<sub>A</sub> site. A comparative analysis of the nqi tensors from His-M219 N<sub>δ</sub> of SQ<sub>A</sub>, histidine N<sub>δ</sub> nitrogen donors of other semiquinone-binding proteins, and imidazole–copper complexes reveals that the protonated nitrogens of the imidazoles in these systems share similar valence electron occupancies. By adopting the Townes–Daley model developed previously for the model copper complex imidazole nitrogens<sup>17</sup> and applying it to the semiquinones, the asymmetry parameter  $\eta$  is developed as an indicator of the hydrogen bond strength. The isotropic hfi coupling constant  $a(^{14}\text{N})$  is found to correlate remarkably well with  $\eta$ , and the two coupling constants are proposed as a measure of the histidine N<sub>δ</sub>–semiquinone H-bond strength, with support from previous computational studies as well as our own DFT calculations.

## EXPERIMENTAL SECTION

**Sample Preparation.** Reaction centers used in this study were isolated from a strain of *Rb. sphaeroides* expressing RCs with a histidine-tag on the M subunit.<sup>18</sup> Cells were grown under the natural abundance of <sup>14</sup>N or in uniformly <sup>15</sup>N-labeled media by substitution with labeled ammonium sulfate obtained from Cambridge Isotopes. To remove the broad signal arising from the magnetic coupling of the semiquinone to the high spin Fe<sup>2+</sup>, the iron was biochemically replaced with diamagnetic Zn<sup>2+</sup> according to the procedures outlined by Utschig et al.<sup>19</sup> Argon gas was slowly blown over the samples to achieve semianaerobic conditions, after which 10 mM dithionite was added to generate SQ<sub>A</sub>. Samples were then promptly frozen in liquid nitrogen.

**ESEEM and ENDOR Experiments.** The instrumentation, pulse sequences, and spectral processing for X-band one-dimensional (1D) three-pulse ESEEM ( $\pi/2-\tau-\pi/2-T-\pi/2-\tau$ -echo) and two-dimensional (2D) four-pulse ESEEM (HYSCORE) ( $\pi/2-\tau-\pi/2-t_1-\pi-t_2-\pi/2-\tau$ -echo) were as described previously.<sup>20</sup> Q-band measurements were carried out on an Oxford CF 935 cryostat equipped with an EN 5107D2 resonator. The repetition rate for all pulse sequences was 1000 Hz. HYSCORE data sets were collected in the form of 2D time-domain patterns containing 256 × 256 points with 20 or 32 ns steps. Spectral processing of ESEEM patterns, including subtraction of the relaxation decay (fitting by 3–6 degree polynomials), apodization (Hamming), zero filling, and fast Fourier transformation (FT), was performed using the Bruker WIN-EPR software. Pulsed ENDOR spectra were acquired using the Davies ( $\pi-t-\pi/2-\tau-\pi-\tau$ -echo) and Mims ( $\pi/2-\tau-\pi/2-t-\pi/2-\tau$ -echo) sequences with a radio-frequency  $\pi$ -pulse inserted during the time interval *t*. The specifics of these experiments are described both in the text and in detail elsewhere.<sup>21</sup>

**Powder <sup>15</sup>N ESEEM and ENDOR Spectra.** The high-resolution pulsed EPR techniques, ESEEM and ENDOR, are sensitive to interactions between the SQ and nearby magnetic nuclei of the protein, the aqueous solvent, and the quinone molecule itself. Pulsed EPR can be used to explore in detail the influence of the environment on the electronic structure of the SQ through the geometry of H-bonds and substituents, via the isotropic and anisotropic hyperfine interactions with magnetic nuclei such as <sup>1</sup>H and <sup>15</sup>N.<sup>10,13</sup> For a hyperfine coupled <sup>15</sup>N nucleus with nuclear spin  $I = 1/2$ , there are only two transitions with frequencies  $\nu_\alpha$  and  $\nu_\beta$ , corresponding to the two different spin states  $m_s = \pm 1/2$  of the SQ electron spin in a constant applied magnetic field. The frequencies depend on the vector sum of the applied magnetic field and the local magnetic field induced at the nucleus by the isotropic and anisotropic hyperfine interactions with the electron spin.

In this work we use X- and Q-band pulsed EPR with microwave frequencies ~9.7 and ~34 GHz, respectively. The X-band EPR spectrum of the SQ in frozen solutions produces a single line with unresolved *g*-tensor anisotropy. The spectral width is comparable to the excitation width of the microwave pulse. Therefore, pulses can be considered as giving a complete excitation of the EPR spectrum, and the ESEEM and ENDOR powder spectra exhibit nuclear frequencies from all orientations of the applied magnetic field relative to the <sup>15</sup>N hfi tensor principal axes. On the other hand, at Q-band the principal components of the SQ *g*-tensor are partially resolved, allowing for orientation selective measurements by exciting only one

section of the EPR spectrum at a time. The combined knowledge from selective (Q-band) and nonselective (X-band) methods can provide an accurate estimate of the principal values and directions of the  $^{15}\text{N}$  hfi tensor. For a powder spectrum, the frequencies of the  $\nu_\alpha$  and  $\nu_\beta$  transitions span the range between

$$\nu_{\alpha(\beta)\perp} = |\nu^{15}\text{N} \pm A_\perp/2| \quad \text{and} \quad \nu_{\alpha(\beta)\parallel} = |\nu^{15}\text{N} \pm A_\parallel/2| \quad (1)$$

which correspond to the perpendicular and parallel orientations of the axial hfi tensor, respectively.  $\nu^{15}\text{N}$  is the Zeeman frequency of  $^{15}\text{N}$  in the applied magnetic field, and  $A_\perp = |a - T|$  and  $A_\parallel = |a + 2T|$  (where  $a$  and  $T$  are the isotropic and anisotropic hyperfine coupling constants, respectively). The full axial hyperfine tensor has principal components ( $a - T$ ,  $a - T$ ,  $a + 2T$ ). The principal values for a rhombic hfi tensor are defined as ( $a - T(1 + \delta)$ ,  $a - T(1 - \delta)$ ,  $a + 2T$ ) where  $\delta$  is the rhombic parameter (which ranges in value from 0 to 1).

Powder HSCORE spectra of  $I = 1/2$  nuclei reveal, in the form of cross-ridges, the interdependence of  $\nu_\alpha$  and  $\nu_\beta$  at a given orientation. For strongly isotropic couplings, the two coordinates at the maximum intensity of the cross-ridge can be used for the first-order estimate of the hyperfine coupling by taking the difference of the nuclear transitions from opposite spin manifolds ( $\nu_\alpha - \nu_\beta$ ). This method for approximating the hfi also applies for weak couplings in powder ENDOR spectra.

**Powder  $^{14}\text{N}$  ESEEM Spectra.** Because of the  $I = 1$  spin and the quadrupole interactions resulting from this, a  $^{14}\text{N}$  nucleus can produce up to six lines in an ESEEM spectrum, three for each of the two electron spin manifolds  $m_S = \pm 1/2$ . In measurements of amorphous (powder) samples, such as the frozen suspensions of RCs used in this work, not all transitions contribute equally to the spectrum due to different orientation dependences. The ESEEM spectrum expected from  $^{14}\text{N}$  with a predominantly isotropic hyperfine coupling is governed by the ratio between the effective nuclear frequency in each manifold,  $\nu_{\text{eff}\pm} = |\nu^{14}\text{N} \pm |A(^{14}\text{N})|/2|$ , and the quadrupole coupling constant (qcc),  $K = e^2Qq/4h$ .<sup>22,23</sup>

If  $\nu_{\text{eff}\pm}/K \sim 0$ , i.e.,  $\nu_{\text{eff}\pm} \sim 0$  (the situation known as the cancellation condition, because  $\nu_N \approx A/2$ ), the three nuclear frequencies of the corresponding manifold will be close to the three pure (zero-field) nuclear quadrupole resonance frequencies with  $^{14}\text{N}$  transitions

$$\nu_+ = K(3 + \eta) \quad \nu_- = K(3 - \eta) \quad \nu_0 = 2K\eta \quad (2)$$

and with the energy levels defined by the principal values of the nqi tensor

$$Q_{\min} = -K(1 - \eta) \quad Q_{\text{mid}} = -K(1 + \eta) \quad Q_{\max} = 2K \quad (3)$$

where  $Q_{\min}$  and  $Q_{\max}$  are the lowest and highest magnitude components, respectively. Both eq 2 and eq 3 are completely described by  $K$  and the asymmetry parameter  $\eta$ . These frequencies, with the property  $\nu_+ = \nu_- + \nu_0$ , are broadened as  $\nu_{\text{eff}\pm}/K$  departs from 0 but can appear in the spectrum up to a ratio of  $\nu_{\text{eff}\pm}/K \sim 0.75$ –1.<sup>22,23</sup>

If  $\nu_{\text{eff}\pm}/K > 1$ , only a single line is expected, without pronounced orientation dependence from each corresponding manifold. This line is produced by a transition at the maximum frequency, which is actually a double-quantum transition between the two nuclear outer states with  $m^{14}\text{N} = -1$  and  $+1$ . The frequency of this transition is well described by<sup>22</sup>

$$\nu_{\text{dq}\pm} = 2[\nu_{\text{eff}\pm}^2 + K^2(3 + \eta^2)]^{1/2} \quad (4)$$

A three-pulse ESEEM spectrum near the cancellation condition is expected to consist of four lines: three narrow lines at zero-field nqi frequencies from the manifold with  $\nu_{\text{eff}\pm} \sim 0$  (eq 2), and one broadened double-quantum transition  $\nu_{\text{dq}\pm}$  from the opposite manifold. Because  $\nu_{\text{dq}\pm}$  is from the manifold not satisfying the cancellation condition, it may be too broad to observe in the three-pulse ESEEM spectrum. However, the corresponding HSCORE spectrum will exhibit cross-peaks correlating  $\nu_+$ ,  $\nu_-$ , and  $\nu_0$  with  $\nu_{\text{dq}\pm}$  indicating the location of  $\nu_{\text{dq}\pm}$  even if it is not directly observed. The cross-peak contour line shapes are expected to be narrow ridges parallel to one coordinate axis and perpendicular to the other. The narrowness of the cross-peaks in one dimension over the other reflects the sharpness of lines near the cancellation condition ( $\nu_+$ ,  $\nu_-$ , and  $\nu_0$ ) as opposed to the nuclear transition not satisfying the cancellation condition ( $\nu_{\text{dq}\pm}$ ). The total number of possible cross-peaks from one nitrogen in each quadrant is nine pairs,<sup>24</sup> but additional combination peaks can appear in multinuclear systems. These combination peaks can only exist at locations that correspond to the sum or difference of nuclear transition frequencies from different  $^{14}\text{N}$  nuclei within the same manifold. On the other hand, when the nitrogen couplings are far from the cancellation condition, the HSCORE spectrum is expected to greatly simplify into that of a single pair of cross-peaks correlating the double-quantum transitions from opposite spin manifolds ( $\nu_{\text{dq}+}$  and  $\nu_{\text{dq}-}$ ).

**Spectral Simulations.** ESEEM and ENDOR simulations were performed in the g-tensor frame of  $\text{SQ}_A$  with EasySpin v4.5.5 in Matlab R2013b.<sup>25</sup> The principal axes of the g-tensor ( $X$ ,  $Y$ ,  $Z$ ) with respect to the molecular frame of the quinone have been defined by single-crystal EPR experiments for  $\text{SQ}_A$ <sup>9</sup> and are shown in Figure 1. The orientations of the hfi and nqi tensor principal axes for  $\text{N}_\delta$  of His-M219 and  $\text{N}_\rho$  of Ala-M260 were related to the g-tensor axes with Euler angles ( $\alpha$ ,  $\beta$ , and  $\gamma$ ) defined by the EasySpin program (<http://www.easyspin.org>). For X-band simulations the excitation bandwidth was assumed fully excitatory, so ideal strong pulses were used.

In the case of Q-band simulations, a careful determination of the effective excitation bandwidth at each field position is important to accurately simulate the orientation selective spectra. This is done by considering the two major contributions to the excitation bandwidth as outlined by EasySpin: the broadening of the EPR spectrum and the selectivity of the microwave pulses. The EPR broadening was determined by simulating the Q-band continuous wave spectrum (Figure S1, Supporting Information). The excitation bandwidth of the pulses was estimated by multiplying the inverse of the initial microwave  $\pi$ -pulse by two for Davies ENDOR. For HSCORE, the excitation bandwidth was optimized during the simulation process.

A characteristic feature of Davies ENDOR is the suppression of small couplings. This was taken into account in our simulations by applying the weighting function<sup>26</sup>

$$\frac{A(^{15}\text{N})^2}{A(^{15}\text{N})^2 + \left(\frac{0.7}{t_p}\right)^2} \quad (5)$$

which approaches zero and one for small and large values of  $A(^{15}\text{N})$ , respectively. Note that use of a longer pulse length  $t_p$  for the first microwave  $\pi$ -pulse reduces the suppression of



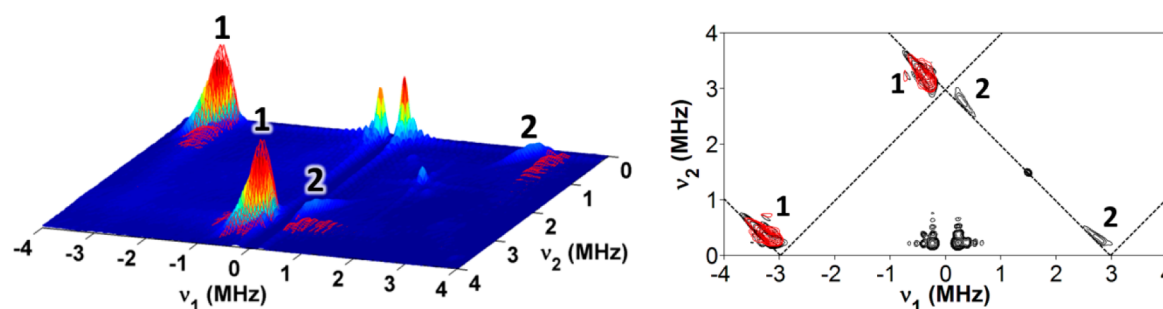


**Figure 2.** Comparison of the experimental and simulated X-band  $^{15}\text{N}$  HYSCORE spectrum of  $\text{SQ}_\text{A}$ . The spectrum is presented in stacked (left) and contour (right) modes. The dashed lines in the contour representation are defined by  $|\nu_1 \pm \nu_2| = 2(\nu^{15}\text{N})$ . Simulation of feature 1 is shown in red (Table 1). Experimental parameters: magnetic field = 345.9 mT, time between first and second pulses  $\tau = 136$  ns, microwave frequency = 9.702 GHz, temperature = 80 K.

weaker couplings. Simulations were also weighted to account for the fact that our radio-frequency generator does not supply a constant power output over the frequency range 2–9 MHz, leading to artificial attenuation of the low frequency peaks. This was approximately corrected for by multiplying the simulations with a simple linear function to match the relative intensities of the low and high frequency peaks observed in the experimental spectra.

All other parameters were the same as those used in the experiments. Optimization of the parameters was done by simultaneous fitting of all spectra. Therefore, the simulation parameters were judged by their ability to reproduce all experimental spectra, as opposed to just one.

**DFT Calculations.** The DFT calculations were performed using the B3LYP functional. The EPR-II basis set was used for all atoms except Zn where 6-31g(d) was employed. The model for the calculations was the QM portion of the QM/MM optimized geometry, as described previously.<sup>16</sup> All calculations were performed using the ORCA electronic structure program.<sup>27</sup> For the quadrupole coupling calculations we used the default ORCA  $^{14}\text{N}$  quadrupole moment value of 0.01930 barn.

## RESULTS

**X-Band  $^{15}\text{N}$  HYSCORE.** The X-band  $^{15}\text{N}$  HYSCORE spectrum for  $\text{SQ}_\text{A}$  is shown in Figure 2. The spectrum contains features 1 and 2, located in the (+/−) and (+/+) quadrants, which appear to be two well-resolved nitrogen couplings that satisfy the cancellation condition ( $\nu^{15}\text{N} \approx |A(^{15}\text{N})|/2$ ). From the locations of the cross-peak maxima (−3.23, +0.37) MHz (1) and (+2.74, +0.33) MHz (2) the first-order estimates of the hyperfine couplings are 3.60 and 2.41 MHz, respectively (2.57 and 1.72 MHz when scaled to  $^{14}\text{N}$ ). However, the reliability of this simple analysis is called into question by the unusual features of the spectrum. The cross-peak arcs are close to the coordinates (0,  $2\nu^{15}\text{N}$ ) and ( $2\nu^{15}\text{N}$ , 0), which, in regard to the HYSCORE intensity, correspond to a singularity for the perpendicular direction or a simple maximum for the parallel orientation of the hfi tensor.<sup>28</sup> Peaks in this region of the HYSCORE spectrum ( $|\nu_{1(2)}| < 0.2$  MHz) are also subject to strong suppression and broadening effects, which complicate the analysis. In Figure 2, the peaks exhibit a curvature not in accordance with the theoretically predicted line shape for a single  $I = 1/2$  anisotropic hfi.<sup>28</sup> Overlap from multiple  $^{15}\text{N}$  couplings may explain these distortions, as simulations of features 1 and 2 as separate nitrogens failed to reproduce the relative peak intensities (as discussed in more detail later).

**Q-Band  $^{15}\text{N}$  ENDOR and HYSCORE.** The spectral complications at X-band are likely a consequence of the cancellation condition being met for the coupled nitrogens. This can be avoided by selecting a different microwave frequency, which changes the resonant magnetic field, and consequently the nitrogen Zeeman frequency  $\nu^{15}\text{N}$  as well, without affecting the hfi. In this work,  $^{15}\text{N}$  Davies ENDOR and HYSCORE measurements on  $\text{SQ}_\text{A}$  were performed at Q-band ( $\sim 34$  GHz), a frequency range 3–4 times higher than X-band.

Q-band Davies ENDOR was acquired at eight evenly spaced field positions spanning  $g_\text{x}$ ,  $g_\text{y}$ , and  $g_\text{z}$  of the field-swept two-pulse echo (Figure 3). The resulting orientation selective

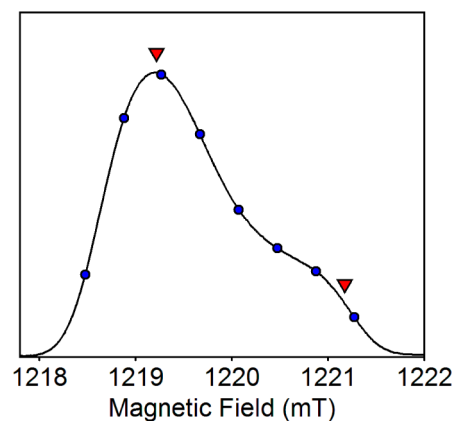


**Figure 3.** Field-swept two-pulse echo of  $\text{SQ}_\text{A}$  at Q-band.  $g_\text{z}$  is resolved at the higher field position  $\sim 1221$  mT, whereas  $g_\text{x}$  and  $g_\text{y}$  form an unresolved pair at  $\sim 1219$  mT. Circles mark the field positions used for Davies ENDOR measurements. Triangles mark the orientations of the external magnetic field in-plane with the  $g_\text{x}/g_\text{y}$  axes (1219.2 mT) and along the unique  $g_\text{z}$  axis (1221.2 mT) used for HYSCORE measurements. Experimental parameters:  $\pi/2$ -pulse length = 120 ns, time between the first and second pulses  $\tau = 500$  ns, microwave frequency = 34.222 GHz, temperature = 80 K.

Davies ENDOR spectra in Figure 4 show only a single resolvable splitting with an average hyperfine coupling of  $\sim 3.4$  MHz. However, the Davies pulse sequence can lead to suppression of weaker couplings, so Mims ENDOR (which is specifically sensitive to small couplings) was performed to ensure that no features were missed in the Davies ENDOR spectrum (Figure S2, Supporting Information). No additional peaks were observed in the Mims experiment.

Of the three principal components of the  $\mathbf{g}$ -tensor, only  $g_\text{z}$  is resolved in the field-swept echo pattern (Figure 3). In this case,

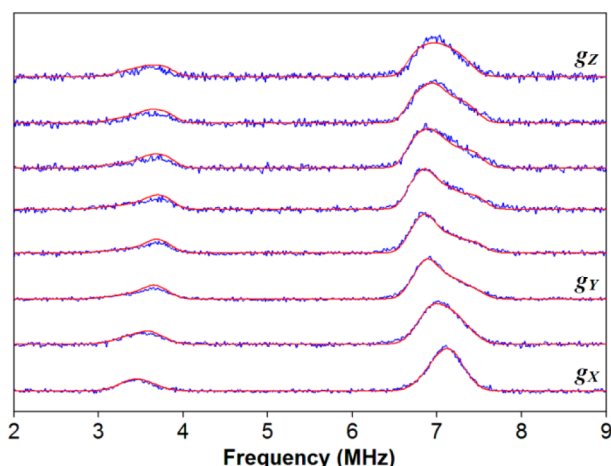


**Figure 4.** Q-band  $^{15}\text{N}$  Davies ENDOR spectra of  $\text{SQA}$ . Traces were taken at eight field positions from 1218.5 mT (bottom trace,  $g_X$ ) to 1221.3 mT (top trace,  $g_Z$ ) in steps of 0.4 mT. The experimental data are shown in blue and are overlaid by the simulations in red (Table 1). Experimental parameters: microwave  $\pi/2$ -pulse length = 120 ns, time between first and second pulses  $\tau$  = 500 ns, RF  $\pi$ -pulse length = 70  $\mu\text{s}$ , microwave frequency = 34.222 GHz, temperature = 80 K.

$g_Z$  is the most single-crystal-like orientation and is expected to give the narrowest peaks in comparison with measurements at other field positions. However, this is not observed in the Davies ENDOR spectrum and, instead, the field position most closely associated with  $g_X$  produces the narrowest line width. This suggests that the spectrum may be the overlap of multiple nitrogen peaks with couplings more similar along  $g_X$  than they are along  $g_Z$ .

Q-band  $^{15}\text{N}$  HSCORE was performed at orientations of the external magnetic field in-plane with the  $g_X/g_Y$  axes and along the  $g_Z$  axis (Figures 3 and 5). Compared with the X-band  $^{15}\text{N}$  HSCORE spectrum (Figure 2), increasing the microwave frequency to Q-band greatly simplifies the spectrum to that of a

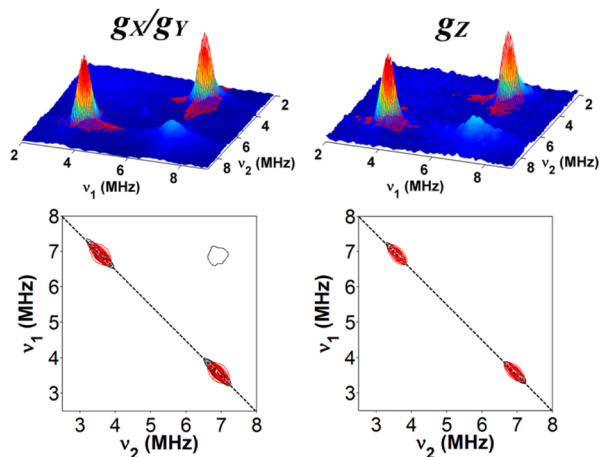


**Figure 5.** Comparison of the experimental and simulated Q-band  $^{15}\text{N}$  HSCORE spectra of  $\text{SQA}$  at orientations of the external magnetic field in-plane with the  $g_X/g_Y$  axes (left) and along the  $g_Z$  axis (right). Spectra are presented in stacked (top) and contour (bottom) modes. The dashed line in the contour representation is defined by  $|\nu_1 + \nu_2| = 2(\nu_{^{15}\text{N}})$ . Simulations are shown in red (Table 1). Experimental parameters: time between first and second pulses  $\tau$  = 136 ns, microwave frequency = 34.217 GHz,  $\pi/2$ -pulse length = 28 ns, temperature = 80 K.

single pair of cross-peaks. The cross-peak maxima are at (3.59, 6.92) MHz in both spectra. These coordinates give a first-order estimate of the hyperfine coupling as 3.33 MHz (2.38 MHz when scaled to  $^{14}\text{N}$ ).

**Q-Band  $^{15}\text{N}$  ENDOR and HSCORE Simulations.** The Q-band  $^{15}\text{N}$  Davies ENDOR and HSCORE spectra were simulated under the assumption that the observed  $\sim 3.4$  MHz splitting belongs to both His-M219  $\text{N}_\delta$  and Ala-M260  $\text{N}_\beta$ . This is supported by previous studies showing these two nitrogens to both closely satisfy the cancellation condition.<sup>14,15</sup> Because the nitrogen couplings are unresolved in all of our  $^{15}\text{N}$  spectra, a purely experimental determination of the two hfi tensors was not possible. Therefore, the Euler angles, which define the principal axes of the hfi tensors in the  $\text{SQA}$  g-tensor coordinate system for the two nitrogens, were generated from our ORCA calculations and fixed throughout the simulations. This is justified by the success of DFT to reproduce the experimental Euler angles for the nitrogen hfi tensors in the  $\text{QB}$  site,<sup>29</sup> as well as the excellent agreement between our simulations (using the calculated angles) and the orientation selective Davies ENDOR spectra (Figure 4). For an unambiguous determination of the His-M219  $\text{N}_\delta$  and Ala-M260  $\text{N}_\beta$  hfi principal directions, amino acid specific  $^{15}\text{N}$  isotope labeling would be necessary.

Although some rhombicity in the hfi is expected, no substantial improvement in the simulations was observed when allowing for rhombic hfi tensors, so axial tensors ( $\delta = 0$ ) were assumed in order to reduce the number of parameters. This assignment of axial hfi tensors for the  $\text{SQA}$  nitrogens is supported by our DFT calculations. Furthermore, simulations of the Davies ENDOR spectra showed that neither of the nitrogen couplings can have  $\delta > 0.5$ . Without amino acid specific  $^{15}\text{N}$  isotope labeling to separate the two nitrogen contributions to the spectra, at present we can only conclude that  $\delta$  is within the range 0–0.5 for both nitrogens. With the Euler angles fixed to the ORCA calculated values, only  $a(^{14}\text{N})$  and  $T$  were allowed to vary. Isotropic couplings are expected to arise from unpaired spin density transferred to the nitrogen 2s orbital. Dipole–dipole interactions with the SQ and spin density on the nitrogen p-orbitals are possible sources of anisotropic coupling. These magnetic interactions are expected to result in  $a(^{14}\text{N})$  and  $T$  having the same relative signs, so simulations were performed under this constraint.<sup>30</sup> This was also found to be the case for the nitrogen couplings in the  $\text{QB}$  site.<sup>29</sup>

Simulations with the Euler angles fixed to the DFT calculated values were optimized starting from two initial conditions: one in which His-M219  $\text{N}_\delta$  possessed the larger of the two isotropic couplings and the other in which Ala-M260  $\text{N}_\beta$  had the larger coupling. We found that assignment of Ala-M260  $\text{N}_\beta$  to the higher value of  $a(^{14}\text{N})$  gave better agreement with the experimental Davies ENDOR spectra. Simulations were first adjusted by hand under the assumption that Ala-M260  $\text{N}_\beta$  has the larger coupling  $a(^{14}\text{N})$ , and then the parameters were fine-tuned by least-squares minimization. Only the higher frequency feature ( $\sim 7$  MHz) was considered in the least-squares optimization (Figure 4). The opposite case, where His-M219  $\text{N}_\delta$  had the larger of the two couplings, failed to reproduce the experimentally observed narrower peak width at  $g_X$  than at  $g_Z$  (Figure S3, Supporting Information). Therefore, Ala-M260  $\text{N}_\beta$  was assigned as the stronger of the two nitrogen couplings. The results are summarized in Table 1 with all values recalculated for  $^{14}\text{N}$ .

**Table 1.** Hyperfine Simulation Parameters for SQ<sub>A</sub> and SQ<sub>B</sub> (<sup>15</sup>N Data Recalculated for <sup>14</sup>N) with DFT Calculated Values in Parentheses<sup>a</sup>

quinone	residue	<i>a</i> (MHz) <sup>b</sup>	<i>T</i> (MHz) <sup>b</sup>	$\delta$	Euler angles <sup>c</sup>
Q <sub>A</sub>	His-M219 N <sub>δ</sub>	2.3 (2.7)	0.3 (0.3)	0.0–0.5 (0.0)	[−, 120°, 0°]
	Ala-M260 N <sub>p</sub>	2.6 (1.8)	0.3 (0.3)	0.0–0.5 (0.0)	[−, 130°, −160°]
Q <sub>B</sub> <sup>d</sup>	His-L190 N <sub>δ</sub>	1.3–1.4 (1.3)	0.3–0.4 (0.3)	0.5–0.6 (0.0)	[60°, 110°, −10°]
	Gly-L225 N <sub>p</sub>	0.4 (0.6)	0.2 (0.2)	0.0 (0.0)	[−, 130°, −100°]

<sup>a</sup>Principal values of the rhombic hfi tensor:  $a - T(1 + \delta)$ ,  $a - T(1 - \delta)$ ,  $a + 2T$ ;  $\delta$  ranges from 0 to 1 corresponding to axial and rhombic tensors, respectively. The signs of  $a$  and  $T$  cannot be determined in these experiments. <sup>b</sup>The errors of the coupling constants determined in this work are  $\pm 0.1$  MHz. <sup>c</sup>Hfi tensors with  $\delta = 0$  only require the  $\beta$  and  $\gamma$  Euler angles for their full description, so  $\alpha$  was set as 0 in these cases but is shown as “−”. <sup>d</sup>Parameters determined in a previous work.<sup>29</sup>

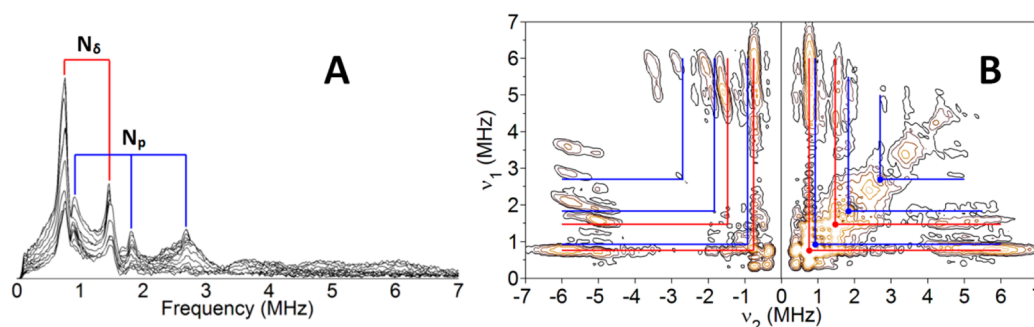


**Figure 6.** (A) Stacked representation of the X-band <sup>14</sup>N three-pulse ESEEM spectra for SQ<sub>A</sub> with nqi triplets corresponding to His-M219 N<sub>δ</sub> (red) and Ala-M260 N<sub>p</sub> (blue) marked. The time between the first and second pulses  $\tau$  was incremented from 100 to 564 ns in steps of 16 ns in successive traces. Experimental parameters: magnetic field = 345.7 mT, microwave frequency = 9.707 GHz, temperature = 80 K. (B) Contour representation of the X-band <sup>14</sup>N HYSCORE spectrum of SQ<sub>A</sub> with diagonal and cross-peak features marked for His-M219 N<sub>δ</sub> (red) and Ala-M260 N<sub>p</sub> (blue). A full 3D view of the spectrum is available in Supporting Information (Figure S4). Experimental parameters: magnetic field = 345.7 mT, time between first and second pulses  $\tau$  = 136 ns, microwave frequency = 9.704 GHz, temperature = 80 K.

The X- and Q-band <sup>15</sup>N HYSCORE spectra calculated with the values in Table 1 are shown in red in Figures 2 and 5, respectively. For the Q-band data sets, the experimental and simulated peak maxima are in excellent agreement (Table S1, Supporting Information). However, only feature 1 of the X-band HYSCORE spectrum is reproduced (Figure 2). Even after exploring potential combination peaks with the proton couplings and the effect of nonideal pulses, the weak intensity feature 2 was not reproduced by the simulations.

**X-Band <sup>14</sup>N Three-Pulse ESEEM.** The X-band <sup>14</sup>N three-pulse ESEEM spectra of SQ<sub>A</sub> measured over a wide range of  $\tau$ -values are shown in stacked presentation in Figure 6A. Two sets of <sup>14</sup>N peaks satisfying the cancellation condition ( $\nu_{\pm} \approx |\nu_{\text{N}}|/2$ ) are present in the spectrum. The most intense set of features ( $\sim 0.75$  MHz, 1.5 MHz) can be assigned to a nqi triplet, as in eq 2, under the assumption that the low frequency peak is a superposition of  $\nu_{-}$  and  $\nu_0$ . When these two lines overlap, the nqi tensor is fully rhombic (principal values:  $-2K$ , 0,  $2K$ ) with an asymmetry parameter  $\eta \approx 1$ . Under this condition the qcc follows the relationship  $\nu_{+} = 4K = e^2qQ/h = 1.5$  MHz, or  $K = 0.38$  MHz.

Also resolved in the three-pulse spectrum is a second, less intense, set of peaks at (0.9, 1.8, 2.7) MHz that define  $K = 0.75$  MHz and  $\eta = 0.6$ . The two qccs  $K = 0.38$  MHz and  $K = 0.75$  MHz are consistent with typical values reported for the protonated nitrogen of an imidazole ring and a peptide nitrogen, respectively. In agreement with previous observations and X-ray structures, these nitrogens can be assigned to N<sub>δ</sub> of His-M219 and N<sub>p</sub> of Ala-M260, respectively. The ratios of  $\nu_{\text{ef-}}/K$  calculated from the hyperfine couplings and qccs for the two nitrogens are smaller than 0.75–1, justifying the appearance of the nqi triplets (or doublet in the case of  $\eta \sim 1$ ) in our powder-

type three-pulse spectra.<sup>22,23</sup> On the other hand, three-pulse ESEEM does not allow for a determination of the relationship between a particular set of nqi frequencies and their corresponding double-quantum transition from the opposite spin manifold ( $\nu_{\text{dq+}}$ ) that could provide an independent estimate of the hyperfine coupling.

**X- and Q-Band <sup>14</sup>N HYSCORE.** When examining spectra with complicated quadrupole features, it is often valuable to combine knowledge obtained from the complementary three-pulse ESEEM and HYSCORE techniques. HYSCORE can resolve peaks missing from three-pulse ESEEM and can correlate peaks associated with the same nucleus, whereas three-pulse spectra can provide the values for nqi transitions in a simpler, easier to identify, format. The three-pulse spectrum of SQ<sub>A</sub> shows two distinct nqi triplets, indicating cancellation conditions are exactly or nearly being met. In this case it is expected that the HYSCORE spectrum will show correlations from the three nqi transitions  $\nu_{+}$ ,  $\nu_{-}$ , and  $\nu_0$  with  $\nu_{\text{dq+}}$  from the opposite manifold.

The representative X-band <sup>14</sup>N HYSCORE spectrum of SQ<sub>A</sub> is shown in Figure 6B. The cancellation condition is strongly satisfied, giving rise to a spectrum of remarkable complexity compared with the simple <sup>14</sup>N HYSCORE spectrum observed previously for SQ<sub>B</sub> away from cancellation at X-band.<sup>29</sup> Peaks with frequencies corresponding to the nqi transitions in the three-pulse ESEEM spectrum lie along the diagonal in the (+/+) quadrant. In general, no diagonal peaks should be observed in HYSCORE. However, they often appear as a result of incomplete inversion of electron spin magnetization by the  $\pi$ -pulse. These frequencies are marked by red (His-M219 N<sub>δ</sub>) and blue (Ala-M260 N<sub>p</sub>) circles along the diagonal. The straight lines that are drawn from the diagonal peaks in the (+/+) quadrant



quadrant pass through ridges of raised intensity located at 4–7 MHz. These straight ridges correlate the single-quantum ( $\sim 0.75$  MHz) and double-quantum (1.5 MHz) peaks from His-M219  $N_\delta$  to the double-quantum transition in the opposite electron spin manifold ( $\nu_{dq+}$ ). Similar features exist for Ala-M260  $N_p$  in this region but are of significantly weaker intensity. This may be due to nuclear cross-suppression effects<sup>31</sup> or the typically large value of  $K$  for peptide nitrogens, which was found previously to suppress the peptide peaks in  $^{14}\text{N}$  spectra of  $\text{SQ}_B$ .<sup>29</sup> Overall, the large number of cross-peaks produces an extremely congested X-band  $^{14}\text{N}$  HYSCORE spectrum, and is further complicated by the presence of combination peaks.

The complexity of the X-band  $^{14}\text{N}$  HYSCORE spectrum is largely attributable to the cancellation condition being satisfied and can be avoided by performing the experiment at a different microwave frequency. The  $^{14}\text{N}$  HYSCORE spectra measured at Q-band are presented in stacked and contour representations in Figure 7. The spectra are dramatically simplified in comparison

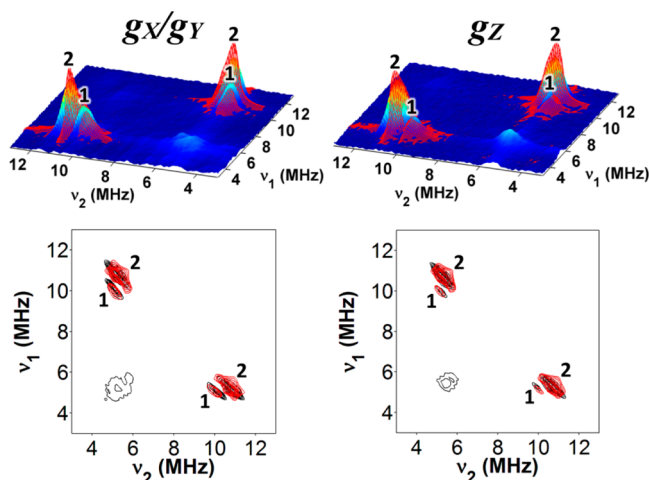


**Figure 7.** Comparison of the experimental and simulated Q-band  $^{14}\text{N}$  HYSCORE spectra of  $\text{SQ}_A$  at orientations of the external magnetic field in-plane with the  $g_x/g_y$  axes (left) and along the  $g_z$  axis (right). Spectra are presented in stacked (top) and contour (bottom) modes. Simulations are shown in red (Tables 1 and 2). Experimental parameters: time between first and second pulses  $\tau = 136$  ns, microwave frequency = 34.112 GHz,  $\pi/2$ -pulse length = 28 ns, temperature = 90 K.

with Figure 6B and have a similar appearance to the X-band  $^{14}\text{N}$  HYSCORE spectrum of  $\text{SQ}_B$  where the nitrogen couplings are far from cancellation.<sup>29</sup> Only two pairs of cross-peaks are observed, with maxima at (10.20, 5.01) MHz (1) and (10.88, 5.11) MHz (2) at  $g_x/g_y$ , and (9.95, 5.25) MHz (1) and (10.78, 5.20) MHz (2) at  $g_z$ . These coordinates correlate the double-quantum transitions  $\nu_{dq+}$  and  $\nu_{dq-}$  for each coupled nitrogen.

The Q-band  $^{14}\text{N}$  HYSCORE spectrum can serve as a test of our assignment of Ala-M260  $N_p$  as the larger of the two nitrogen hyperfine couplings. With the values of  $K$  and  $\eta$  determined from the X-band three-pulse ESEEM spectra,  $\nu_{dq+}$  can be predicted from eq 4 for the cases where His-M219  $N_\delta$  or Ala-M260  $N_p$  has the larger of the two  $a(^{14}\text{N})$  values in Table 1. If His-M219  $N_\delta$  were to have the larger value of  $a(^{14}\text{N})$ , then identical  $\nu_{dq+}$  transitions at  $\sim 10.2$  MHz ( $N_\delta$ ) and  $\sim 10.2$  MHz ( $N_p$ ) would be expected. If the larger value were to belong to Ala-M260  $N_p$ , then well-resolved transitions at  $\sim 9.9$  MHz ( $N_\delta$ ) and  $\sim 10.4$  MHz ( $N_p$ ) should be present in the Q-band  $^{14}\text{N}$

HYSCORE spectrum. Only the latter scenario is consistent with the observed peak arrangement, and therefore His-M219  $N_\delta$  is assigned to 1 and Ala-M260  $N_p$  to 2 in Figure 7. Simulations provide further support of this assignment, with the experimental and simulated peak maxima in strong agreement (Table S2, Supporting Information).

**$^{14}\text{N}$  Three-Pulse and HYSCORE Simulations.**  $^{14}\text{N}$  three-pulse ESEEM simulations were performed for eight evenly spaced values of  $\tau$ . The initial values for  $K$  and  $\eta$  were determined from the analysis of Figure 6A under the assumption of near cancellation for both nitrogens. Simultaneous simulation alongside the Q-band  $^{14}\text{N}$  HYSCORE spectra (Figure 7), as well as the  $^{15}\text{N}$  HYSCORE and ENDOR spectra, was done iteratively until a parameter set was obtained that could reproduce the general features of all of the experimental data considered.

The orientation of the principal axes of the nqi tensor with respect to the molecular frame has been discussed in detail previously for  $N_\delta$  of His-L190 and  $N_p$  of Gly-L225 H-bonded to  $\text{SQ}_B$ .<sup>29</sup> For a SQ H-bonded to the  $N_\delta$  of a histidine, it was concluded that for weaker hydrogen bonding,  $Q_{\text{max}}$  will orient perpendicular to the imidazole plane, whereas for stronger H-bonds  $Q_{\text{max}}$  will exchange with the  $Q_{\text{mid}}$  direction and become parallel to the imidazole plane.<sup>32</sup> His-M219  $N_\delta$  of  $\text{SQ}_A$  ( $\eta \approx 1$ ) represents the special case where these two possible nqi tensor orientations are indistinguishable. In the simulations, the nqi tensor orientation was assigned on the basis of best agreement with our DFT calculations, with  $Q_{\text{max}}$  parallel to the imidazole plane,  $Q_{\text{mid}}$  perpendicular to the imidazole plane, and  $Q_{\text{min}}$  along the N–H bond.

The nqi tensor characteristics of the peptide nitrogen are only slightly perturbed by hydrogen bonding, as has been confirmed by theoretical works.<sup>33–35</sup> From these calculations, it was found that the  $Q_{\text{max}}$  principal direction is normal to the local peptide plane, the  $Q_{\text{mid}}$  direction almost coincides with the C(O)–N(H) bond, and  $Q_{\text{min}}$  points about  $30^\circ$  off of the N–H bond. Our DFT calculations were in good agreement with the assigned orientations of the  $N_\delta$  and  $N_p$  nqi tensors for  $\text{SQ}_A$  (Table 2 and Figures S5 and S6, Supporting Information). The Euler angles for the His-M219  $N_\delta$  and Ala-M260  $N_p$  nqi tensors were therefore generated from crystal structure 1DV3 and fixed throughout the simulations.

A comparison of the experimental and simulated  $^{14}\text{N}$  three-pulse ESEEM spectra is shown in Figure 8. The final hfi and nqi parameters optimized by simultaneous simulation of the  $^{14,15}\text{N}$

**Table 2. Nuclear Quadrupole Simulation Parameters for  $\text{SQ}_A$  and  $\text{SQ}_B$  with DFT Calculated Values in Parentheses**

nitrogen	$K$ (MHz) <sup>a</sup>	$\eta$ <sup>a</sup>	Euler angles
$N_\delta$ His-M219	0.38 (0.36)	0.97 (0.57)	$[-130^\circ, 100^\circ, -100^\circ]$ $([-130^\circ, 100^\circ, -100^\circ])$
$N_p$ Ala-M260	0.74 (−0.99)	0.59 (0.45)	$[170^\circ, 80^\circ, -110^\circ]$ $([140^\circ, 80^\circ, -110^\circ])$
$N_\delta$ His-L190 <sup>b</sup>	0.38–0.39 (0.40)	0.69 (0.57)	$[170^\circ, 30^\circ, -10^\circ]$ $([-120^\circ, 80^\circ, -100^\circ])$
$N_p$ Gly-L225 <sup>b</sup>	0.74 (−0.98)	0.45 (0.47)	$[-120^\circ, 60^\circ, -160^\circ]$ $([-160^\circ, 60^\circ, -160^\circ])$

<sup>a</sup>See Tables 5 and 6 for a more detailed analysis of the calculated quadrupole tensors. The errors associated with the values of  $K$  and  $\eta$  determined in this work are  $\pm 0.1$  MHz and  $\pm 0.03$ , respectively. The sign of  $K$  cannot be determined in these experiments. <sup>b</sup>Parameters determined in previous work. The DFT calculated values for  $\eta$  were reported incorrectly previously.<sup>29</sup>

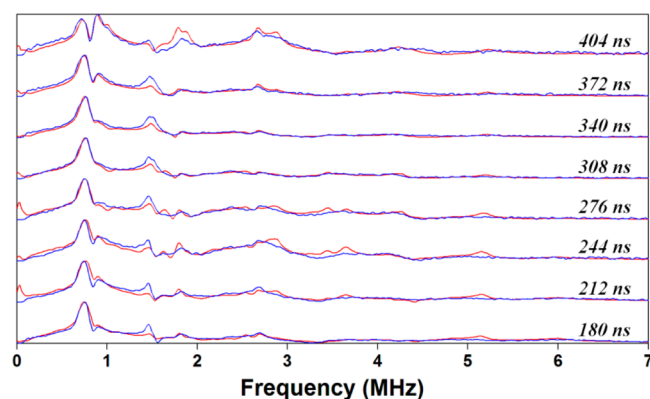


**Figure 8.** Comparison of the experimental (blue) and simulated (red) X-band  $^{14}\text{N}$  three-pulse ESEEM spectra of  $\text{SQ}_\text{A}$  (Tables 1 and 2).  $\tau$ -values chosen were evenly spaced starting from 180 ns in the bottom trace and increased in steps of 32 ns in subsequent traces. Experimental parameters: magnetic field = 345.7 mT, microwave frequency = 9.707 GHz, temperature = 80 K.

ESEEM and  $^{15}\text{N}$  ENDOR spectra, together with our DFT calculated values for  $\text{SQ}_\text{A}$  (and  $\text{SQ}_\text{B}$  for comparison), are summarized in Tables 1 and 2. A full 3D view of the hfi tensor alignments to the molecular frame determined from DFT calculations is available in the Supporting Information (Figure S7). The X-band  $^{14}\text{N}$  HYSCORE spectrum was not included in the simulations due to complications arising from the many combination lines, as well as the presence of intense diagonal peaks that cannot be simulated with ideal pulses.

## DISCUSSION

**Comparison with Previous Results.** X-band three-pulse  $^{14}\text{N}$  ESEEM spectra of  $\text{SQ}_\text{A}$  were previously reported by Hoff and co-workers.<sup>14,15</sup> However, only long pulse delay times,  $\tau \geq 260$  ns, were utilized, leaving substantial uncertainties in the measured nqi tensor parameters and estimates of the hyperfine coupling. To ensure that the data set is complete and reproducible over a large range of  $\tau$ , it is valuable to create a quasi-2D ESEEM spectrum by stacking sequential  $\tau$  values. This type of representation masks  $\tau$  dependent suppression effects and accentuates true peaks. The three-pulse ESEEM spectra (Figure 6A) were accumulated at  $\tau$ -values incremented in 16 ns steps starting from 100 to 564 ns (measurements were also performed with a 50 ns step size to ensure that relevant features at long times were not missed).

The spectrum is in reasonable agreement with previously published results.<sup>14,15</sup> However, in contrast to the earlier work, in which separate peaks at 0.64 and 0.85 MHz were seen, we observe a single feature centered at  $\sim 0.75$  MHz constituting the overlap of the  $\nu_-$  and  $\nu_0$  nqi transitions for His-M219  $\text{N}_\delta$ . We adjusted our sample preparation according to the protocol of

Spoyalov et al.,<sup>15</sup> but the resulting spectra were not significantly different from that shown in Figure 6A, with no splitting of the feature centered at  $\sim 0.75$  MHz. Instead, our work is in agreement with Lendzian et al., in which the  $^{14}\text{N}$  three-pulse ESEEM spectrum of  $\text{SQ}_\text{A}$  shows an unresolved feature at  $\sim 0.75$  MHz.<sup>36</sup>

**Variation in the hfi and nqi Tensors of Histidine  $\text{N}_\delta$  Donors in Different Quinone Sites.** In this section we perform a comparative analysis of the hfi and nqi tensor characteristics for the histidine  $\text{N}_\delta$  H-bond donors of semiquinones in several different quinone sites. Currently available data from the literature are shown in Table 3. Only nqi tensors determined from three-pulse ESEEM spectra with at least one resolvable single-quantum transition are shown, so as to consider only the most accurate determinations of  $\eta$ . The coupling constants listed in Table 3 vary within a factor of  $\sim 3$  for  $a(^{14}\text{N})$ , a  $\sim 25$ – $30\%$  range for  $e^2Qq/h$ , and a factor of  $\sim 2$  for  $\eta$ .

The relationship between the values in Table 3 and the quinone site geometry was investigated using available crystal structures. In this work, we adopt the same in-plane and out-of-plane angle definitions introduced by Fritscher (Figure S8, Supporting Information).<sup>32</sup> The  $\text{N}\cdots\text{O}$  distance and the in-plane ( $\theta$ ) and out-of-plane ( $\phi$ ) angles describing the position of the carbonyl oxygen with respect to the histidine  $\text{N}_\delta$  were estimated from the crystal structures and are listed in Table 4. The quinone site geometry is very similar across all X-ray structures considered, although small differences are observed for the  $\text{Q}_\text{D}$  site from NarGHI, a nitrate reductase from *E. coli*. However, the NarGHI structure is in complex with inhibitor pentachlorophenol rather than the native menaquinone-8, which is a “quinol-like” structure and likely a poor representation of the bound SQ state. Nevertheless, no clear correlation is found between the geometrical parameters listed in Table 4 and the values  $a(^{14}\text{N})$  and  $\eta$  in Table 3.

The nqi characteristics for imidazole  $\text{N}_\delta$  and  $\text{N}_\epsilon$  have been extensively studied in several series of similar compounds with specifically varying characteristics. For the amine  $\text{N}_\delta$  and the imine  $\text{N}_\epsilon$  coordinating the metal in zinc, cadmium, and copper imidazole model compounds and copper proteins, a pronounced linear correlation between  $h/e^2qQ$  and  $\eta$  has been found. The slopes of these correlations vary within a narrow range  $\sim 0.34 \pm 0.05 \text{ MHz}^{-1}$ .<sup>17,40</sup>

An explanation of the linear dependence of  $h/e^2qQ$  vs  $\eta$  was developed in the context of the Townes–Dailey model,<sup>41</sup> on the basis of a consideration of the electron population of the bonding orbitals of the nitrogen by p electrons. This analysis assumes that the geometry of the nitrogen molecular environment does not change between different systems, and this is likely true within the same class of compounds. However, significant deviations from linearity have been reported for some compounds, and in one case have been assigned to

**Table 3.** hfi and nqi Coupling Constants for Histidine  $\text{N}_\delta$  Hydrogen Bonded to Semiquinones

quinone site	residue	$a(^{14}\text{N})$ (MHz)	$e^2Qq/h$ (MHz)	$\eta$	refs
$\text{Q}_\text{A}$ <i>Rb. sphaeroides</i>	M219 $\text{N}_\delta$	2.3	1.50	0.97	this work
$\text{Q}_\text{A}$ <i>Rp. viridis</i>	M217 $\text{N}_\delta$	$\sim 2$	1.51 <sup>a</sup>	0.87 <sup>a</sup>	37
$\text{Q}_\text{A}$ PSII	D214 $\text{N}_\delta$	1.67–1.9	1.47–1.58	0.71–0.78	30, 38
$\text{Q}_\text{B}$ <i>Rb. sphaeroides</i>	L190 $\text{N}_\delta$	1.3–1.4	1.50–1.54	0.69	29
$\text{Q}_\text{D}$ NarGHI	C66 $\text{N}_\delta$	0.8	1.96	0.5	39

<sup>a</sup>We have reanalyzed the spectra on the basis of the assigned peak positions.



Table 4. Geometry of the Histidine N<sub>δ</sub> with Respect to the SQ in Available Crystal Structures

quinone site	quinone	number of structures	N...O distance (Å)	in-plane angle $\theta$ (deg) <sup>a</sup>	out-of-plane angle $\phi$ (deg) <sup>a</sup>
Q <sub>A</sub> <i>Rb. sphaeroides</i>	UQ-10	47	2.80 ± 0.15	−3 ± 4	−3 ± 10
Q <sub>A</sub> <i>Rp. viridis</i>	MQ-9	14	2.84 ± 0.12	−5 ± 3	2 ± 7
Q <sub>A</sub> PSII <i>vulcanus</i> <sup>b</sup>	PQ-9	4	2.71 ± 0.09	−2 ± 6	−12 ± 1
Q <sub>B</sub> <i>Rb. sphaeroides</i>	UQ-10	20	2.69 ± 0.21	−9 ± 7	−5 ± 8
Q <sub>D</sub> NarGHI	MQ-8 <sup>c</sup>	1	2.84	26	−19

<sup>a</sup>Angle definitions for  $\theta$  and  $\phi$  are provided in the Supporting Information (Figure S8). <sup>b</sup>Distances and angles reported for PSII are from *Thermosynechococcus vulcanus*, whereas the corresponding ESEEM data in Table 3 are for RCs isolated from spinach. <sup>c</sup>The crystal structure is in complex with inhibitor pentachlorophenol instead of menaquinone-8, so the hydroxyl group of PCP was used for the distance and angle measurements.

external influences on the distal amine nitrogen, in particular due to hydrogen bonds.<sup>40</sup>

The dependence observed between  $h/e^2qQ$  and  $\eta$  is reproduced in Figure 9 for copper diene-substituted imidazole

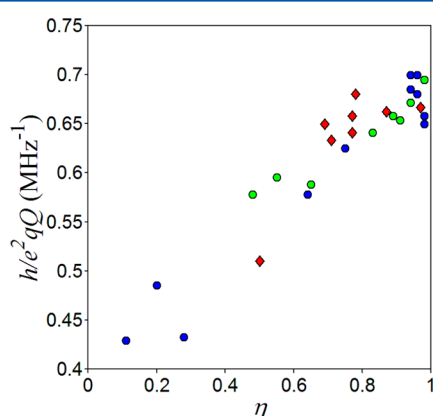


**Figure 9.** Dependence of  $h/e^2qQ$  on  $\eta$  for available semiquinone (Table 3) and copper complex data. The data for copper diene-substituted imidazole model compounds (blue) and copper proteins (green) are shown as circles. The histidine N<sub>δ</sub> data for the semiquinones are shown as red diamonds.

model compounds and copper proteins.<sup>17</sup> Also shown are the histidine-N<sub>δ</sub> qccs for the semiquinones from Table 3, which are confined to the same area as that of the copper complexes.

Fritscher explored computationally the changes in  $e^2qQ/h$  and  $\eta$  of the N<sub>δ</sub> nitrogen as a function of H-bond geometry using methylimidazole–benzosemiquinone as a model system.<sup>32</sup> A variety of different conformations of the semiquinone with respect to the imidazole were tested. Rotation of the semiquinone about its axis defined by the carbonyl oxygens had essentially no effect on the nqi tensor, and changes to the in-plane ( $\theta$ ) and out-of-plane ( $\phi$ ) angles describing the orientation of the carbonyl oxygen with respect to N<sub>δ</sub> only amounted to changes in  $\eta$  up to 0.1. Because  $\theta$  and  $\phi$  in Table 4 are generally well-conserved across the crystal structures considered, variations in these angles cannot explain the wide range in  $\eta$  for the semiquinones listed in Table 3.

Though the relative orientations of methylimidazole and benzosemiquinone had little impact on the N<sub>δ</sub> nqi tensor, Fritscher found the hydrogen bond length to have a dramatic effect on  $\eta$  (Figure S9, Supporting Information).<sup>32</sup> Shortening the N...O distance from 3.25 to 2.75 Å resulted in an increase in  $\eta$  from 0.17 to 0.61. This corresponds to a decrease in magnitude of the  $Q_{\max}$  tensor component oriented perpendicular to the imidazole plane, coupled to an increase in the  $Q_{\text{mid}}$  component lying in-plane with the imidazole ring. Between

2.75 and 2.50 Å,  $\eta$  reaches its maximum value of 1, where  $|Q_{\text{mid}}| = |Q_{\max}|$  by definition (eq 3). A further shortening of the H-bond led to a situation where the component perpendicular to the imidazole plane was no longer largest in magnitude, resulting in a reorientation of the nqi tensor with  $Q_{\max}$  in-plane with the imidazole ring. Under this new definition of the nqi tensor,  $\eta$  decreased in response to further shortening of the H-bond, resulting in  $\eta = 0.72$  at 2.50 Å. The total change in  $\eta$  from shortening the N...O distance from 3.25 Å ( $\eta = 0.17$ ) to 2.50 Å ( $\eta = 0.72$ ) can be calculated as  $(1 - 0.17) + (1 - 0.72) = 1.11$  (when taking into account that  $\eta$  passes through 1, see Figure S9, Supporting Information). This analysis shows that the range of  $\eta$  in Table 3 is very likely accounted for by differences in H-bond length, and not by variations in  $\theta$  or  $\phi$  (Table 4). The fact that  $\eta$  is selectively sensitive to the histidine N<sub>δ</sub>–semiquinone N...O distance makes it promising as a molecular ruler of the H-bond length. However, the N<sub>δ</sub> nqi tensor orientations for the semiquinones must first be known before  $\eta$  can be taken full advantage of.

For His-M219 N<sub>δ</sub> of SQ<sub>A</sub> in *Rb. sphaeroides*,  $\eta \approx 1$ , corresponding to the special case where either nqi tensor definition described above is appropriate. However,  $\eta$  is significantly less than 1 for the other semiquinone data in Table 3, so the tensor orientations for these N<sub>δ</sub> nitrogens must be determined explicitly. In our previous work on SQ<sub>B</sub>, we found that simulations with  $Q_{\max}$  oriented either in-plane or perpendicular to the imidazole ring fit the <sup>14</sup>N ESEEM spectra equally well, preventing an unambiguous assignment of the nqi tensor orientation.<sup>29</sup> In the present work, the nqi tensor orientations for the semiquinone data in Table 3 are determined from a comparative analysis of the asymmetry parameter  $\eta$  and the isotropic hyperfine constant  $a(^{14}\text{N})$  for each histidine N<sub>δ</sub> nitrogen.

The isotropic hyperfine constant  $a(^{14}\text{N})$  for the histidine N<sub>δ</sub> nitrogens from Table 3 is plotted as a function of  $\eta$  in Figure 10. A remarkably good linear correlation is observed for all quinone sites considered. A larger hyperfine coupling (indicative of a stronger hydrogen bond) is found to correlate with a larger value of  $\eta$ . Because His-M219 N<sub>δ</sub> of SQ<sub>A</sub> (*Rb. sphaeroides*) has the largest value of  $a(^{14}\text{N})$ , the other semiquinones are likely engaged in weaker hydrogen bonding with the histidine. Therefore, the nqi tensors for the other semiquinone data in Table 3 can be assigned as having  $Q_{\max}$  oriented perpendicular to the imidazole plane, in accordance with the calculations of Fritscher described above.<sup>32</sup> This nqi tensor orientation is consistent with that determined previously for the copper diene-substituted imidazole model compounds and copper proteins (plotted alongside the semiquinone data in Figure 9).<sup>17</sup>

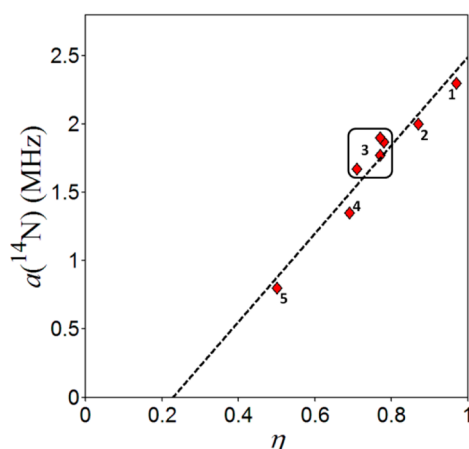


**Figure 10.** Correlation between  $a(^{14}\text{N})$  and  $\eta$  for the semiquinone  $\text{N}_\delta$  data in Table 3: (1)  $\text{Q}_\text{A}$  *Rb. sphaeroides*; (2)  $\text{Q}_\text{A}$  *Rp. viridis*; (3)  $\text{Q}_\text{A}$  PSII; (4)  $\text{Q}_\text{B}$  *Rb. sphaeroides*; (5)  $\text{Q}_\text{D}$  NarGHI. The linear fit to the  $\text{N}_\delta$  data (dashed line) is described by  $a(^{14}\text{N}) = 3.23\eta - 0.74$  (MHz).

The strong correlation between  $a(^{14}\text{N})$  and  $\eta$  in Figure 10 is unexpected, as the hyperfine coupling is sensitive to both the relative orientation and H-bond distance of the histidine  $\text{N}_\delta$ –semiquinone couple. The nitrogen hyperfine coupling was calculated by Konstantinos et al.<sup>42</sup> on the methylimidazole–benzosemiquinone model system as a function of angular perturbations (such as rotation of the semiquinone about its  $g_x$  axis and changes to the out-of-plane angle  $\phi$ ), and changes to the H-bond distance (where a decrease in the  $\text{O}\cdots\text{H}$  distance from  $\sim 3$  to  $\sim 2$  Å resulted in an approximately linear increase in spin transfer to the coupled nitrogen). All geometrical perturbations were found to have a significant impact on the isotropic coupling and were more than sufficient to cover the range of values listed in Table 3.<sup>42</sup> Therefore, we attribute the remarkably good correlation observed between  $a(^{14}\text{N})$  and  $\eta$  in Figure 10 to a well-conserved binding geometry of the semiquinones with their histidine  $\text{N}_\delta$  H-bond donors in the quinone sites considered. A similar conformation of the SQs in the quinone sites of the homologous reaction center proteins is not unexpected (Table 4). However, a similar binding geometry is also implicated for the nitrate reductase NarGHI, which shares no homology with the other proteins. This suggests the existence of a more generally conserved histidine  $\text{N}_\delta$ –semiquinone H-bond motif in Nature. Thus,  $a(^{14}\text{N})$ , like  $\eta$ , may also be a good indicator of the hydrogen bond distance (and strength) when all other aspects of the relative geometry between the semiquinone and the histidine remain the same. Figure 10 can thus act as a molecular ruler to estimate the relative histidine  $\text{N}_\delta$ –semiquinone H-bond strengths for the available semiquinone data, where a higher value of  $a(^{14}\text{N})$  or  $\eta$  corresponds to a stronger hydrogen bond. This trend is consistent with the relative anisotropic coupling constants ( $T$ ) determined for the histidine  $\text{N}_\delta$  H-bond proton couplings for the  $\text{Q}_\text{A}$  and  $\text{Q}_\text{B}$  semiquinones from *Rb. sphaeroides* previously.<sup>16</sup> The empirical relationship is also in agreement with observed changes in the nqi tensor as a function of N–H bond distance (determined from neutron diffraction data) in a series of model imidazole and histidine compounds.<sup>43</sup>

**DFT Modeling of the Histidine and Peptide Nitrogen nqi Tensors.** A more detailed analysis of the DFT calculated nqi tensors for our  $\text{Q}_\text{A}$  site model allows us to probe more deeply into the electronic structure around the  $^{14}\text{N}$  nucleus, in

particular focusing on changes occurring as a result of hydrogen bonding. In Table 5 we compare the calculated nqi tensor principal values for  $\text{N}_\delta$  of the four histidines ligated to the  $\text{Zn}^{2+}$  ion in metal-exchanged RCs.

**Table 5.** Calculated nqi Tensors and NH Bond Lengths for  $\text{N}_\delta$  in the Histidine Ligands of the  $\text{Zn}^{2+}$  Ion

	$Q_\text{p}$ (MHz) <sup>a</sup>	$Q_\text{NH}$ (MHz) <sup>b</sup>	$Q_\text{pl}$ (MHz) <sup>c</sup>	$\eta$	NH (Å)
His-M219 $\text{N}_\delta$ <sup>d</sup>	−1.14	−0.32	1.45	0.57	1.05
His-M266 $\text{N}_\delta$	−2.36	1.41	0.95	0.19	1.00
His-L190 $\text{N}_\delta$	−2.32	1.45	0.86	0.25	1.01
His-L230 $\text{N}_\delta$	−2.32	1.45	0.86	0.25	1.01

<sup>a</sup>nqi tensor component perpendicular to the imidazole ring plane. <sup>b</sup>nqi tensor component along the NH bond. <sup>c</sup>nqi tensor component orthogonal to  $Q_\text{p}$  and  $Q_\text{NH}$  and in-plane with the imidazole ring (see caption of Figure S9 (Supporting Information) for more details). <sup>d</sup>The optimized  $\text{N}\cdots\text{O}$  distance from the histidine  $\text{N}_\delta$  nitrogen to the semiquinone carbonyl oxygen was 2.7 Å

In the computational model used, the protonated  $\text{N}_\delta$  on His-M219 is involved in hydrogen bond donation to  $\text{SQ}_\text{A}$ , whereas the other three histidine residues are not H-bonded. Table 5 shows that for the three histidine ligands without any hydrogen bonding, the nqi values are all very similar, with the largest magnitude (negative) component perpendicular to the imidazole plane,  $Q_\text{p}$ . The other two principal values are positive with the larger component along the N–H bond,  $Q_\text{NH}$ . This is illustrated graphically in Figure 11a for His-L230. Identical plots are obtained for  $\text{N}_\delta$  of histidines L190 and M266.

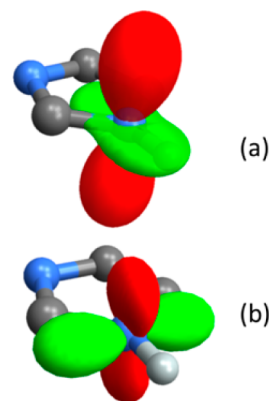


**Figure 11.** Polar plots of the calculated nqi tensors for  $\text{N}_\delta$  in the imidazole groups of (a) His-L230 and (b) His-M219. The nqi tensor is plotted as a surface map showing the sign and symmetry visually, with red representing negative and green representing positive principal values; see ref 44 for further details of this representation of tensors.

Hydrogen bond formation of the semiquinone anion radical with  $\text{N}_\delta$  of His-M219 leads to a significant lengthening of the N–H bond. This causes an approximate halving in the magnitude of  $Q_\text{p}$ ,  $Q_\text{NH}$  to become opposite in sign, and the in-plane component  $Q_\text{pl}$  to almost double in magnitude.  $Q_\text{pl}$  is now the largest magnitude principal value. The graphical representation in Figure 11b clearly demonstrates these effects on the nqi tensor components and, in particular, the dramatic reduction in magnitude of  $Q_\text{NH}$  caused by the hydrogen bond to  $\text{SQ}_\text{A}$ . A straightforward interpretation is that the polarization of the N–H bond upon hydrogen bond formation leads to an

increased electron density in its  $sp^2$  hybrid orbital. This interpretation is in agreement with the trends observed for the electron occupancies of the nitrogen  $sp^2$ - and  $p$ -orbitals as a function of H-bond strength found for copper diene-substituted imidazole model compounds and L-histidine hydrochloride monohydrate.<sup>17,45</sup> The increased electron density along N–H leads to a more negative contribution to  $Q_{NH}$  while at the same time producing a positive contribution to both  $Q_p$  and  $Q_{pl}$ . The increased  $s$  unpaired electron spin density at the  $N_\delta$  nucleus also promotes a stronger isotropic hyperfine coupling.

In Table 5, the calculated  $\eta$  values for each residue are also given and show the sensitivity of  $\eta$  to hydrogen bonding. The experimentally determined  $\eta = 0.97$  for M219  $N_\delta$  is considerably larger than the calculated value given in Table 5. This suggests that one principal component is near zero with the other two similar in magnitude but opposite in sign. On the basis of the effect of hydrogen bonding demonstrated in Table 5, this most likely arises from the  $Q_{NH}$  component being near zero. Therefore, our model calculation may overestimate the strength of hydrogen bonding resulting in a more negative contribution to  $Q_{NH}$  than occurs in the real system.

We have performed a similar analysis of the Ala-M260 peptide  $N_p$  group. The  $nqi$  principal values are presented in Table 6, where they are compared with the neighboring  $N_p$

**Table 6. Calculated  $nqi$  Tensors and NH Bond Lengths for the Peptide Nitrogens near Ala-M260  $N_p$**

	$Q_p$ (MHz) <sup>a</sup>	$Q_{NH}$ (MHz) <sup>b</sup>	$Q_{pl}$ (MHz) <sup>c</sup>	$\eta$	NH (Å)
Ala-M260 $N_p$ <sup>d</sup>	−3.95	1.09	2.86	0.45	1.02
Asn-M259 $N_p$	−4.09	1.82	2.32	0.12	1.01
Thr-M261 $N_p$	−4.59	2.04	2.54	0.11	1.01

<sup>a</sup> $nqi$  tensor component perpendicular to the peptide C–N–C plane.

<sup>b</sup> $nqi$  tensor component along the NH bond. <sup>c</sup> $nqi$  tensor component orthogonal to  $Q_p$  and  $Q_{NH}$ . <sup>d</sup>The optimized N...O distance from the peptide nitrogen to the semiquinone carbonyl oxygen was 2.8 Å

groups, which are not hydrogen bonded in the model used. Polar plot representations are provided in the Supporting Information (Figure S10).

For all the peptide  $N_p$  groups, the  $nqi$  principal component with the largest (negative) magnitude is perpendicular to the peptide C–N–C plane,  $Q_p$ . The most notable change upon hydrogen bond formation between  $SQ_A$  and Ala-M260 is a decrease in  $Q_{NH}$ . This can again be explained by a polarization of the nitrogen  $sp^2$  hybrid orbital along the direction of the hydrogen bond, but the calculations indicate a much smaller perturbation of the electronic environment of  $N_p$  compared with that of the histidine  $N_\delta$ . The asymmetry parameter  $\eta$  is again predicted to increase significantly upon hydrogen bond formation, but the increase in N–H bond length caused by hydrogen bonding is less than for the histidine  $N_\delta$ . This analysis is in agreement with the relative hyperfine couplings and asymmetry parameters determined experimentally for the coupled peptide nitrogens of  $SQ_A$  and  $SQ_B$  in Tables 1 and 2. Of the two peptide nitrogens, Ala-M260  $N_p$  has the larger value of  $a(^{14}N)$  (Table 1). This is consistent with the larger value of  $\eta$  for this nitrogen (Table 2), indicating  $SQ_A$  to have the stronger peptide hydrogen bond than  $SQ_B$ .

## CONCLUSION

X- and Q-band  $^{14,15}N$  ESEEM and  $^{15}N$  ENDOR were performed on the  $Q_A$  site of bacterial RCs to characterize the hfi and  $nqi$  between  $SQ_A$  and its two hydrogen bond donors, His-M219  $N_\delta$  and Ala-M260  $N_p$ . Our analysis provides a significant improvement over the  $^{14}N$  hyperfine coupling constants 1.8 and 1.1 MHz estimated previously for His-M219  $N_\delta$  and Ala-M260  $N_p$  by Spoyalov et al.,<sup>15</sup> which were based on an assignment of the double-quantum transition ( $\nu_{dq+}$ ) in their three-pulse ESEEM spectra that is not supported by the present work. This highlights the importance of utilizing 2D correlation spectroscopies for an accurate determination of  $\nu_{dq+}$  when hyperfine couplings are estimated.

Despite the stronger hydrogen bond to His-M219  $N_\delta$  (as established by atom-specific  $^{13}C$  labeling of the ubiquinone molecule acting as  $Q_A$  and modeling of the  $SQ_A$  spin density distribution),<sup>10,16</sup> we find Ala-M260  $N_p$  to have the larger of the two nitrogen hyperfine couplings. This was not predicted by our DFT calculations, which assigned a greater value of  $a(^{14}N)$  to the stronger H-bond donor His-M219  $N_\delta$ . The same trend in relative nitrogen coupling strengths is observed in the  $Q_A$  site of cyanide-treated PSII, where the peptide nitrogen was found to have a larger coupling than that of the histidine H-bond donor.<sup>30</sup> On this basis, it was concluded that the peptide nitrogen provides the stronger of the two hydrogen bonds to the semiquinone.<sup>46</sup> However, our results show that the nitrogen couplings for His-M219  $N_\delta$  and Ala-M260  $N_p$  do not reflect their relative H-bond strengths. Also, DFT calculations on the plastosemiquinone anion radical in PSII found the histidine  $N_\delta$  to be the stronger of the two H-bond donors.<sup>47</sup> Therefore, the previous assignments of the hydrogen bond proton couplings for  $SQ_A$  in PSII are not unambiguous.<sup>46</sup>

From a comparative analysis of available  $nqi$  data for several semiquinone species and for copper complexes,<sup>17</sup> we find that the protonated imidazole nitrogens of these systems share similar valence orbital occupancies. By adopting the Townes–Dailey model used previously for the copper complexes, we propose  $a(^{14}N)$  and  $\eta$  can serve as a molecular ruler of the histidine  $N_\delta$ –semiquinone hydrogen bond strength for systems in which all other aspects of the SQ binding conformation are similar. This conclusion is supported by computational works on model methylimidazole-benzosemiquinone systems,<sup>32,42</sup> as well as our own DFT calculations. The empirical relationships determined here can be used to accurately predict the relative H-bond strengths in semiquinone proteins from a simple analysis of the hfi and  $nqi$  tensor parameters and will provide an important structural characterization tool for future pulsed EPR studies on histidine  $N_\delta$ –semiquinone hydrogen bonding interactions.

## ASSOCIATED CONTENT

### Supporting Information

Tables S1 and S2, simulated and experimental peak maxima of Q-band  $^{14,15}N$  HYSCORE. Figure S1, simulation of the Q-band CW spectrum for estimating the contribution of EPR broadening to the excitation bandwidth. Figure S2, Q-band  $^{15}N$  Mims ENDOR spectrum of  $SQ_A$ . Figure S3, additional Q-band  $^{15}N$  Davies ENDOR simulations of  $SQ_A$ . Figure S4, X-band  $^{14}N$  HYSCORE spectrum of  $SQ_A$  in stacked presentation. Figures S5–S7, orientation of hfi and  $nqi$  tensors for His-M219  $N_\delta$  and Ala-M260  $N_p$ . Figure S8, definition of in-plane ( $\theta$ ) and out-of-plane ( $\phi$ ) angles describing the position of the



semiquinone carbonyl oxygen with respect to the histidine N $\delta$ . Figure S9, calculated dependence of  $\eta$  on the N $\cdots$ O hydrogen bond distance. Figure S10, polar plot of the calculated nqi tensor for peptide NH. This material is available free of charge via the Internet at <http://pubs.acs.org>.

## AUTHOR INFORMATION

### Corresponding Authors

\*P.J.O.: email, [patrick.o'malley@manchester.ac.uk](mailto:patrick.o'malley@manchester.ac.uk); phone, 00441612004536.

\*C.A.W.: We are deeply saddened to report that Professor Colin A. Wraight passed away on July 10, 2014.

\*S.A.D.: email, [dikanov@illinois.edu](mailto:dikanov@illinois.edu); phone, (217) 300-2209.

### Author Contributions

The manuscript was written through contributions of all authors. All authors have given approval to the final version of the manuscript.

### Notes

The authors declare no competing financial interest.

## ACKNOWLEDGMENTS

This research was supported by the DE-FG02-08ER15960 Grant from Chemical Sciences, Geosciences and Biosciences Division, Office of Basic Energy Sciences, Office of Sciences, U.S. Department of Energy, and NIH Grant GM062954 (S.A.D.), NSF Grant MCB-0818121 (C.A.W.), and NCRR/NIH Grant S10-RR15878 and S10-RR025438 for pulsed EPR instrumentation. A.T.T. gratefully acknowledges support as a NIH trainee of the Molecular Biophysics Training Program (5T32-GM008276). P.J.O'M. acknowledges the use of computer resources granted by the EPSRC UK national service for computational chemistry software (NSCCS).

## REFERENCES

- (1) Okamura, M. Y.; Paddock, M. L.; Graige, M. S.; Feher, G. Proton and Electron Transfer in Bacterial Reaction Centers. *Biochim. Biophys. Acta* **2000**, *1458*, 148–163.
- (2) Wraight, C. A. Proton and Electron Transfer in the Acceptor Quinone Complex of Photosynthetic Reaction Centers from *Rhodobacter sphaeroides*. *Front. Biosci.* **2004**, *9*, 309–337.
- (3) Lancaster, C. R. D. The Role of Electrostatics in Proton-Conducting Membrane Protein Complexes. *FEBS Lett.* **2003**, *545*, 52–60.
- (4) Lancaster, C. R. D. Ubiquinone Reduction and Protonation in Photosynthetic Reaction Centres from *Rhodospseudomonas viridis*—X-ray Structures and their Functional Implications. *Biochim. Biophys. Acta* **1998**, *1365*, 143–150.
- (5) Xu, Q.; Gunner, M. R. Exploring the Energy Profile of the Q $_A^-$  to Q $_B$  Electron Transfer Reaction in Bacterial Photosynthetic Reaction Centers: pH Dependence of the Conformational Gating Step. *Biochemistry* **2002**, *41*, 2694–2701.
- (6) Stowell, M. H.; McPhillips, T. M.; Rees, D. C.; Soltis, S. M.; Abresch, E.; Feher, G. Light-Induced Structural Changes in Photosynthetic Reaction Center: Implications for Mechanism of Electron-Proton Transfer. *Science* **1997**, *276*, 812–816.
- (7) Wraight, C. A.; Gunner, M. R. The Acceptor Quinones of Purple Photosynthetic Bacteria – Structure and Spectroscopy. In *The Purple Phototrophic Bacteria*; Hunter, C. N., Daldal, F., Thurnauer, M. C., Beatty, J. T., Eds.; Springer Science + Business Media B.V.: Berlin, 2009; pp 379–405.
- (8) Axelrod, H. L.; Abresch, E. C.; Paddock, M. L.; Okamura, M. Y.; Feher, G. Determination of the Binding Sites of the Proton Transfer Inhibitors Cd $^{2+}$  and Zn $^{2+}$  in Bacterial Reaction Centers. *Proc. Natl. Acad. Sci. U. S. A.* **2000**, *97*, 1542–1549.
- (9) Isaacson, R. A.; Lendzian, F.; Abresch, E. C.; Lubitz, W.; Feher, G. Electronic Structure of Q $_A^-$  in Reaction Centers from *Rhodobacter sphaeroides*. I. Electron Paramagnetic Resonance in Single Crystals. *Biophys. J.* **1995**, *69*, 311–322.
- (10) Lubitz, W.; Feher, G. The Primary and Secondary Acceptors in Bacterial Photosynthesis III. Characterization of the Quinone Radicals Q $_A$  and Q $_B$  by EPR and ENDOR. *Appl. Magn. Reson.* **1999**, *17*, 1–48.
- (11) Lubitz, W. EPR in Photosynthesis. *Electron Paramagn. Reson.* **2004**, *19*, 174–242.
- (12) Schnegg, A.; Dubinskii, A. A.; Fuchs, M. R.; Grishin, Y. A.; Kirilina, E. P.; Lubitz, W.; Plato, M.; Savitsky, A.; Möbius, K. High-Field EPR, ENDOR and ELDOR on Bacterial Photosynthetic Reaction Centers. *Appl. Magn. Reson.* **2007**, *31*, 59–98.
- (13) Dikanov, S. A. Resolving Protein-Semiquinone Interactions by Two-Dimensional ESEEM Spectroscopy. *Electron Paramagn. Resonan.* **2013**, *23*, 103–179.
- (14) Bosch, M. K.; Gast, P.; Hoff, A. J.; Spoyalov, A. P.; Tsvetkov, Y. D. The Primary Acceptor Quinone Q $_A$  in reaction centers of *Rhodobacter Sphaeroides* R26 is Hydrogen Bonded to the N $^{(1)}$ -H of His M219. An Electron Spin Echo Study of Q $_A^-$ . *Chem. Phys. Lett.* **1995**, *239*, 306–312.
- (15) Spoyalov, A. P.; Hulsebosch, R. J.; Shochat, S.; Gast, P.; Hoff, A. J. Evidence that Ala M260 is Hydrogen-Bonded to the Reduced Primary Acceptor Quinone Q $_A^-$  in Reaction Centers of *Rb. Sphaeroides*. *Chem. Phys. Lett.* **1996**, *263*, 715–720.
- (16) Martin, E.; Samoilova, R. I.; Narasimhulu, K. V.; Lin, T. J.; O'Malley, P. J.; Wraight, C. A.; Dikanov, S. A. Hydrogen Bonding and Spin Density Distribution in the Q $_B$  Semiquinone of Bacterial Reaction Centers and Comparison with the Q $_A$  Site. *J. Am. Chem. Soc.* **2011**, *133*, 5525–5537.
- (17) Jiang, F.; McCracken, J.; Peisach, J. Nuclear Quadrupole Interactions in Copper(II)-Diethylenetriamine-Substituted Imidazole Complexes and in Copper(II) Proteins. *J. Am. Chem. Soc.* **1990**, *112*, 9035–9044.
- (18) Goldsmith, J. O.; Boxer, S. G. Rapid Isolation of Bacterial Photosynthetic Reaction Center with an Engineered Polyhistidine Tag. *Biochim. Biophys. Acta* **1996**, *1276*, 171–175.
- (19) Utschig, L. M.; Greenfield, S. R.; Tang, J.; Laible, P. D.; Thurnauer, M. C. Influence of Iron-Removal Procedures on Sequential Electron Transfer in Photosynthetic Bacterial Reaction Centers Studied by Transient EPR Spectroscopy. *Biochemistry* **1997**, *36*, 8548–8558.
- (20) Martin, E.; Samoilova, R. I.; Narasimhulu, K. V.; Wraight, C. A.; Dikanov, S. A. Hydrogen Bonds Between Nitrogen Donors and the Semiquinone in the Q $_B$  Site of Bacterial Reaction Centers. *J. Am. Chem. Soc.* **2010**, *132*, 11671–11677.
- (21) Schweiger, A.; Jeschke, G. *Principles of Pulse Electron Paramagnetic Resonance*; Oxford University Press: Oxford, U.K., 2001.
- (22) Dikanov, S. A.; Tsvetkov, Y. D.; Bowman, M. K.; Astashkin, A. V. Parameters of Quadrupole Coupling of  $^{14}\text{N}$  Nuclei of Chlorophyll *a* Cations Determined by Electron Spin Echo Method. *Chem. Phys. Lett.* **1982**, *90*, 149–153.
- (23) Flanagan, H.; Singel, D. J. Analysis of  $^{14}\text{N}$  ESEEM Patterns of Randomly Oriented Solids. *J. Chem. Phys.* **1987**, *87*, 5606–5616.
- (24) Dikanov, S. A.; Xun, L.; Karpel, A. B.; Tyryshkin, A. M.; Bowman, M. K. The Orientationally-Selected Two-Dimensional ESEEM Spectroscopy of the Rieske-Type Iron-Sulfur Cluster in 2,4,5-Trichlorophenoxyacetate Monooxygenase from *Burkholderia cepacia* AC1100. *J. Am. Chem. Soc.* **1996**, *118*, 8408–8416.
- (25) Stoll, S.; Britt, R. D. General and Efficient Simulation of Pulse EPR Spectra. *Phys. Chem. Chem. Phys.* **2009**, *11*, 6614–6625.
- (26) Fan, C.; Doan, P. E.; Davoust, C. E.; Hoffman, B. M. Quantitative Studies of Davies Pulsed ENDOR. *J. Magn. Reson.* **1992**, *98*, 62–72.
- (27) Neese, F. The ORCA Program System. *Wiley Interdiscip. Rev.: Comput. Mol. Sci.* **2012**, *2*, 73–78.
- (28) Dikanov, S. A.; Bowman, M. K. Cross-Peak Lineshape of Two-Dimensional ESEEM Spectra in Disordered  $S = 1/2$ ,  $I = 1/2$  Spin Systems. *J. Magn. Reson.* **1995**, *116*, 125–128.

- (29) Taguchi, A. T.; O'Malley, P. J.; Wraight, C. A.; Dikanov, S. A. Nuclear Hyperfine and Quadrupole Tensor Characterization of the Nitrogen Hydrogen Bond Donors to the Semiquinone of the Q<sub>B</sub> Site in Bacterial Reaction Centers: A Combined X- and S-band <sup>14,15</sup>N ESEEM and DFT Study. *J. Phys. Chem. B* **2014**, *118*, 1501–1509.
- (30) Deligiannakis, Y.; Hanley, J.; Rutherford, A. W. 1D- and 2D-ESEEM Study of the Semiquinone Radical Q<sub>A</sub><sup>•−</sup> of Photosystem II. *J. Am. Chem. Soc.* **1999**, *121*, 7653–7664.
- (31) Stoll, S.; Calle, C.; Mitrikas, G.; Schweiger, A. Peak Suppression in ESEEM Spectra of Multinuclear Spin Systems. *J. Magn. Reson.* **2005**, *177*, 93–101.
- (32) Fritscher, J. Influence of Hydrogen Bond Geometry on Quadrupole Coupling Parameters: A Theoretical Study of Imidazole–Water and Imidazole–Semiquinone Complexes. *Phys. Chem. Chem. Phys.* **2004**, *6*, 4950–4956.
- (33) Rabbani, S. R.; Edmonds, D. T.; Gosling, P.; Palmer, M. H. Measurement of the <sup>14</sup>N Quadrupole Coupling Constants in Glycine, Diglycine, Triglycine, and Tetraglycine and a Comparison with Calculation. *J. Magn. Reson.* **1987**, *72*, 230–237.
- (34) Palmer, M. H. <sup>14</sup>N Nuclear Quadrupole Coupling in Glycyl-Glycine and Related Peptides. *Z. Naturforsch.* **1984**, *39B*, 1108–1111.
- (35) Elmi, F.; Hadipour, N. L. A Study on the Intermolecular Hydrogen Bonds of α-Glycylglycine in its Actual Crystalline Phase using *ab initio* Calculated <sup>14</sup>N and <sup>2</sup>H Nuclear Quadrupole Coupling Constants. *J. Phys. Chem. A* **2005**, *109*, 1729–1733.
- (36) Lendzian, F.; Rautter, J.; Käß, H.; Gardiner, A.; Lubitz, W. ENDOR and Pulsed EPR Studies of Photosynthetic Reaction Centers: Protein-Cofactor Interactions. *Ber. Bunsen-Ges. Phys. Chem.* **1996**, *100*, 2036–2040.
- (37) Gardiner, A. T.; Zech, S. G.; MacMillan, F.; Käss, H.; Bittl, R.; Schlodder, E.; Lendzian, F.; Lubitz, W. Electron Paramagnetic Resonance Studies of Zinc-Substituted Reaction Centers from *Rhodospseudomonas viridis*. *Biochemistry* **1999**, *38*, 11773–11787.
- (38) Astashkin, A. V.; Hara, H.; Kuroiwa, S.; Kawamori, A.; Akabori, K. A Comparative Electron Spin Echo Envelope Modulation Study of the Primary Electron Acceptor Quinone in Zn-Substituted and Cyanide-Treated Preparations of Photosystem II. *J. Chem. Phys.* **1998**, *108*, 10143–10151.
- (39) Grimaldi, S.; Arias-Cartin, R.; Lanciano, P.; Lyubenova, S.; Endeward, B.; Prisner, T. F.; Magalon, A.; Guigliarelli, B. Direct Evidence for Nitrogen Ligation to the High Stability Semiquinone Intermediate in *Escherichia coli* Nitrate Reductase A. *J. Biol. Chem.* **2010**, *285*, 179–187.
- (40) Ashby, C. I. H.; Cheng, C. P.; Brown, T. L. <sup>14</sup>N Nuclear Quadrupole Resonance Spectra of Coordinated Imidazole. *J. Am. Chem. Soc.* **1978**, *100*, 6057–6063.
- (41) Townes, C. H.; Dailey, B. P. Determination of Electronic Structure of Molecules from Nuclear Quadrupole Effects. *J. Chem. Phys.* **1949**, *17*, 782–796.
- (42) Konstantinos, C. C.; Maria, L.; Rutherford, A. W.; Deligiannakis, Y. Semiquinone in Molecularly Imprinted Hybrid Amino Acid-SiO<sub>2</sub> Biomimetic Materials. An Experimental and Theoretical Study. *J. Phys. Chem. C* **2008**, *112*, 12841–12852.
- (43) Colaneri, M. J.; Peisach, J. An Electron Spin-Echo Envelope Modulation Study of Cu(II)-Doped Single Crystals of L-Histidine Hydrochloride Monohydrate. *J. Am. Chem. Soc.* **1992**, *114*, 5335–5341.
- (44) Autschbach, J.; Zheng, S.; Schurko, R. W. Analysis of Electric Field Gradient Tensors at Quadrupolar Nuclei in Common Structural Motifs. *Concepts Magn. Reson.* **2010**, *36A*, 84–126.
- (45) McDowell, C. A.; Naito, A.; Sastry, D. L.; Takegoshi, K. Determination of the <sup>14</sup>N Quadrupole Coupling Tensor in a Single Crystal of L-Histidine Hydrochloride Monohydrate by NMR Spectroscopy. *J. Magn. Reson.* **1986**, *69*, 283–292.
- (46) Chatterjee, R.; Milikisiyants, S.; Coates, C. S.; Lakshmi, K. V. High-Resolution Two-Dimensional <sup>1</sup>H and <sup>14</sup>N Hyperfine Sublevel Correlation Spectroscopy of the Primary Quinone of Photosystem II. *Biochemistry* **2011**, *50*, 491–501.
- (47) Lin, T. J.; O'Malley, P. J. An ONIOM Study of the Spin Density Distribution of the Q<sub>A</sub> Site Plastosemiquinone in the Photosystem II Reaction Center. *J. Phys. Chem. B* **2011**, *115*, 4227–4233.